



Geophysical Research Letters

RESEARCH LETTER

10.1002/2015GL067028

Key Points:

- The MJO affects vertical propagation of orographic gravity waves over the Tibetan plateau
- Gravity wave breaking is modulated by the MJO's effect on upper-level winds
- The wave drag shifts up and down with MJO phase while the vertically integrated drag is conserved

Supporting Information:

- Texts S1–S5, Figures S1–S4, and Table S1

Correspondence to:

N. Y. Cohen,
ncohen@ldeo.columbia.edu

Citation:

Cohen, N. Y., and W. R. Boos (2016), Modulation of subtropical stratospheric gravity waves by equatorial rainfall, *Geophys. Res. Lett.*, 43, 466–471, doi:10.1002/2015GL067028.

Received 14 NOV 2015

Accepted 17 DEC 2015

Accepted article online 22 DEC 2015

Published online 12 JAN 2016

Modulation of subtropical stratospheric gravity waves by equatorial rainfall

Naftali Y. Cohen¹ and William R. Boos¹

¹Department of Geology Geophysics, Yale University, New Haven, Connecticut, USA

Abstract Internal gravity waves influence a variety of phenomena in Earth's stratosphere and upper troposphere, including aviation weather turbulence and circulations that set high-altitude distributions of ozone and greenhouse gases. Here coupling between the dominant mode of subseasonal variability of the equatorial atmosphere—the Madden-Julian oscillation (MJO)—and subtropical stratospheric gravity waves created by flow over topography is documented for the first time. We use three different meteorological data sets to show that during boreal winter, the MJO modifies the vertical distribution of internal gravity wave drag induced by the Tibetan Plateau and the deposition of momentum into the stratosphere. This interaction, however, has no significant impact on the vertically integrated wave drag. Our findings raise new questions about how future changes in tropical rainfall might affect stratospheric variability and highlight the importance of local processes over Tibet for the circulations that set distributions of climatically important high-altitude trace gases.

1. Introduction

Planetary scale anomalies in winds and precipitation propagate eastward at a speed of about 5 m s^{-1} across the equatorial Indian and Pacific Oceans in a pattern known as the Madden-Julian oscillation (MJO; Figure 1) [Madden and Julian, 1971, 1994]. The MJO is known to affect a range of tropospheric phenomena, influencing the intensity of regional monsoons, the genesis of tropical cyclones, the predictability of midlatitude weather, chemical and biological components of the global climate system, and even the development of the El Niño–Southern Oscillation [Lau and Waliser, 2011; Zhang, 2005]. The effect of the MJO on the stratosphere is less well understood, but work in recent years has shown that subtropical upper tropospheric/lower stratospheric ozone can be modulated by tropical intraseasonal variability [e.g., Liu *et al.*, 2009; Tian and Waliser, 2012]. In addition, other studies have shown that precipitating convection and planetary scale winds in the MJO can produce a variety of equatorially trapped waves (Kelvin, Rossby, and internal gravity waves) that propagate upward across the tropical tropopause into the stratosphere [Weare, 2010; Garfinkel *et al.*, 2012, 2014; Virts and Wallace, 2014]. Yet despite much research on interactions between tropical and extratropical atmospheric phenomena, no clear associations have been established between tropical rainfall and the extratropical waves (Rossby and gravity modes) that propagate upward into the stratosphere. These waves are particularly important because they drive the Brewer-Dobson circulation [Cohen *et al.*, 2014]—the slow overturning of stratospheric air that sets high-altitude distributions of ozone, methane, chlorofluorocarbons, and other trace gases [Butchart, 2014].

Here we show that the MJO affects vertical propagation of topographically induced internal gravity waves over the Tibetan Plateau, the world's largest highland that spans about $2.5 \times 10^6 \text{ km}^2$ in central Asia. Internal gravity waves (hereafter GWs) are produced when stably stratified air flows over obstacles [Bühler, 2014]; these waves can propagate vertically and transport momentum from their source to the region in which they dissipate, consistent with a nonlocal form of Newton's third law in which action is balanced by equal and opposite reaction [Bühler, 2014]. For example, the eastward jet stream exerts an eastward force on the Himalayas and Tibet when it passes over this orography in boreal winter, and the gravity waves that are excited propagate vertically and provide a westward force on the stratosphere when their amplitudes become large enough to nonlinearly and irreversibly mix stratified air (i.e., “break”) at that level. The force transferred by the waves is loosely called a wave “drag” because the waves decelerate the flow toward their phase speed [Andrews *et al.*, 1987], which is zero for orographic GWs. Since most surface flow over orography is eastward, the wave drag

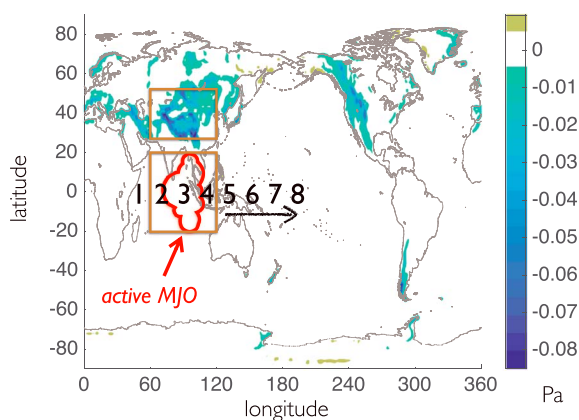


Figure 1. The spatial structure of time-mean gravity wave (GW) drag and MJO precipitation. Shading shows vertically integrated GW drag above 400 hPa (in Pa), averaged over all winters between 1979 and 2012 using the Modern Era Retrospective Analysis for Research and Applications (MERRA) reanalysis data. This shows that the global maximum GW drag lies over Tibet. The numbers 1 to 8 mark the approximate location of maximum precipitation in a particular phase of the MJO as it propagates eastward across the Indian and western central Pacific Oceans. The red line illustrates the location of peak rainfall during MJO phase 3 (an “active” MJO). Brown rectangles mark the integration domains used in Figure 2.

daily data with resolution of about 1.25° in the horizontal and 37 vertical levels that span up to about 0.1 hPa. For the JRA55 reanalysis, we use daily data with resolution of about 1.25° in the horizontal and 42 vertical levels that span up to about 1 hPa. Extrapolated values below Earth’s surface in both reanalyses are omitted from our analysis.

Both reanalysis products approximate the distribution of orographic GWs based on observationally constrained estimates of horizontal wind speeds and densities; no direct observation of the global distribution of orographic GWs exists. Global weather and climate models (GCMs) usually cannot explicitly represent orographic GWs because the 1–10 km horizontal length scales of these waves fall below the typical 100 km horizontal grid spacing of the models, necessitating parameterization of the production, propagation, and breaking of GWs in GCMs [Fritts and Alexander, 2003]. Both MERRA and JRA55 use the GTOPO30 topography data set to obtain the subgrid-scale surface height variance that is used to estimate the GW source.

We also use outgoing longwave radiation (OLR) at the top of the atmosphere as a proxy for precipitating convective activity (reduced OLR signifies enhanced cloud cover and convective motions), with OLR derived from high-resolution infrared radiation sounder observations on board National Oceanic and Atmospheric Administration (NOAA) TIROS-N series and MetOp satellites [Liebmann, 1996]. Here we use daily data with resolution of about 1° in the horizontal. Anomalies in OLR, GW drag, and other variables are computed as the deviation from the corresponding boreal (December–February) mean during the years 1979–2012.

The MJO is classified by values of the Real-time, Multivariate MJO (RMM) index [Wheeler and Hendon, 2004], with components RMM1 and RMM2 that represent the amplitudes of orthogonal perturbations in equatorial cloud amount and winds at upper and lower levels of the troposphere. When the amplitude of the MJO signal in the RMM1-RMM2 phase space is less than one, the MJO is considered weak and it can be difficult to discern MJO location. For amplitudes above one, the MJO is considered strong and there is more certainty in determining the current phase. We refer to the latter as “highly defined” MJO events.

Confidence intervals were assessed using a bootstrap method. Using 34 years of data, we classified each day according to its MJO phase. We then gathered data with the same phase and averaged over a subset of the set of days having a given MJO phase. Each subset has the same size as its parent set, but the elements within it are chosen at random, where repetitions are allowed. We repeat this process 1000 times, which allowed for the computation of the 95% confidence interval about the mean, using empirical quantiles, as shown in

is primarily westward. The Tibetan Plateau and adjacent orography in Asia provide the largest source of GWs and orographic wave drag on Earth (Figure 1).

2. Data and Methods

We investigate covariations in tropical rainfall and subtropical GW breaking during Northern Hemisphere winters (December–February) of 1979–2012 using two different atmospheric reanalysis products: the Modern Era Retrospective Analysis for Research and Applications (MERRA) [Rienecker et al., 2011] and the Japanese 55 year Reanalysis (JRA55) [Kobayashi et al., 2015; Onogi et al., 2007]. MERRA was developed by the Global Modeling and Assimilation Office and supported by the NASA Modeling, Analysis and Prediction Program; we use daily data with resolution of about 1.25° in the horizontal and 42 vertical levels that span up to about 0.1 hPa. For the JRA55 reanalysis, we use daily data with resolution of about 1.25° in the horizontal and 37 vertical levels that span up to about 1 hPa.

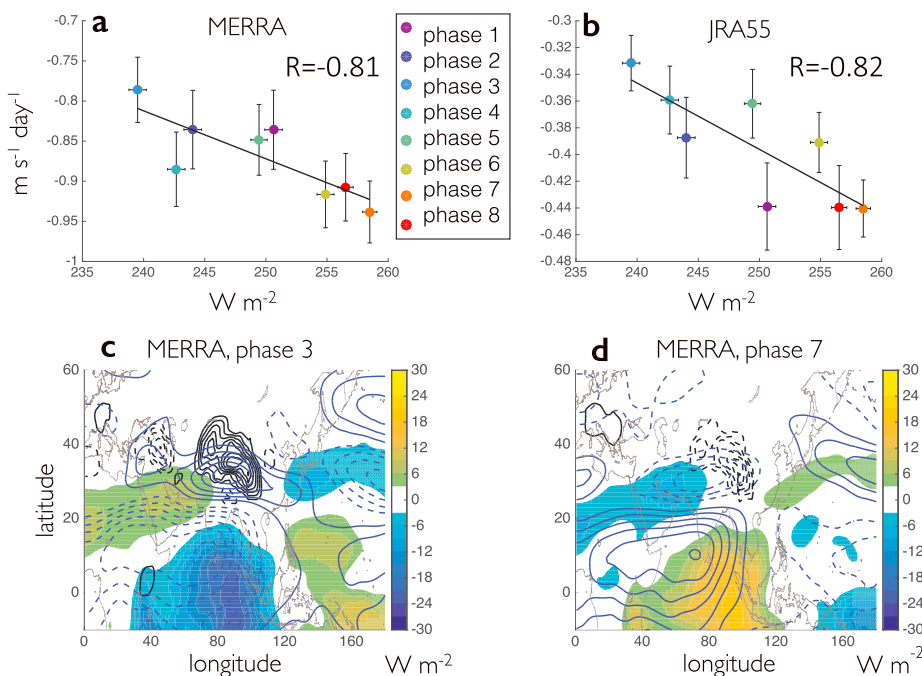


Figure 2. The interaction between the MJO and GW drag over Tibet. (a and b) The relation between GW drag over the Tibetan Plateau (vertical axes) and equatorial NOAA OLR (horizontal axes) in a particular MJO phase using MERRA (Figure 2a) and JRA55 (Figure 2b) GW drag. GW drag is averaged between $60\text{--}120^\circ\text{E}$ and $30\text{--}50^\circ\text{N}$ at 100 hPa , while OLR is averaged between $60\text{--}120^\circ\text{E}$ and $20^\circ\text{S}\text{--}20^\circ\text{N}$ at the top of the atmosphere (brown rectangles in Figure 1). Each dot corresponds to a different MJO phase, and the 95% confidence interval for the mean is marked using the black error bars. Pearson correlation coefficients are shown in each panel, and the linear regression lines are marked too (see section 2). (c and d) Horizontal structures of MJO and GW drag anomalies during MJO phases 3 and 7, respectively, using the MERRA data set. MJO convective activity is indicated by OLR (shading, W m^{-2} , with reduced OLR indicating enhanced cloud cover and precipitation), and upper tropospheric MJO gyres are indicated by 200 hPa eastward wind (blue contours, interval 1 m s^{-1} , negative dashed). Anomalous GW drag at 100 hPa is shown by black contours (interval of $0.05\text{ m s}^{-1}\text{ d}^{-1}$, negative dashed). Only anomalies statistically significant at the 5% level are shown, and values are locally smoothed about $2 \times 2^\circ$ in the horizontal.

Figures 2, 3, and Figures S1 and S2 in the supporting information. Supporting information Table S1 summarizes the statistical analysis of Figures 2a and 2b of the main text and Figure S2 in the supporting information.

3. MJO and GW Drag Interaction

MJO phases associated with enhanced precipitation over the equatorial Indian Ocean are accompanied by modified GW breaking above the Tibetan Plateau, with OLR over the tropical Indian Ocean and the eastward acceleration by GW drag at 100 hPa over Tibet having a Pearson correlation coefficient of about -0.8 when binned by MJO phase (Figures 2a and 2b). Although the range of the composite variations in GW drag at 100 hPa is only about 20% of the mean, fluctuations of GW drag in individual MJO events can be much larger, reaching $\pm 6\text{ m s}^{-1}\text{ d}^{-1}$ (Figure S1 in the supporting information). The linear relationship between tropical OLR and subtropical GW drag across MJO phases is statistically significant in both reanalysis products at a 5% confidence level (Table S1). When we examine only “highly defined” MJO events (see section 2), the correlation decreases slightly to about -0.75 (Figures S2a and S2b); in contrast, when NOAA OLR data are replaced with OLR from the JRA55 and MERRA products, slightly higher correlation coefficients are obtained (about -0.9 in both JRA55 and MERRA data sets, see section 2 and Figures S2c and S2d). This robust statistical relationship is somewhat surprising because the MJO is typically thought of as a tropical phenomenon operating in a domain that is geographically distinct from that of the vertically propagating orographic GWs over Tibet.

To better understand how the MJO modulates orographic GW drag, we examine composite dynamical structures of MJO phases 3 and 7, which have the weakest and strongest GW drag, respectively, at 100 hPa in the MERRA data set (composites of the JRA55 extremes yield similar conclusions and are not shown).

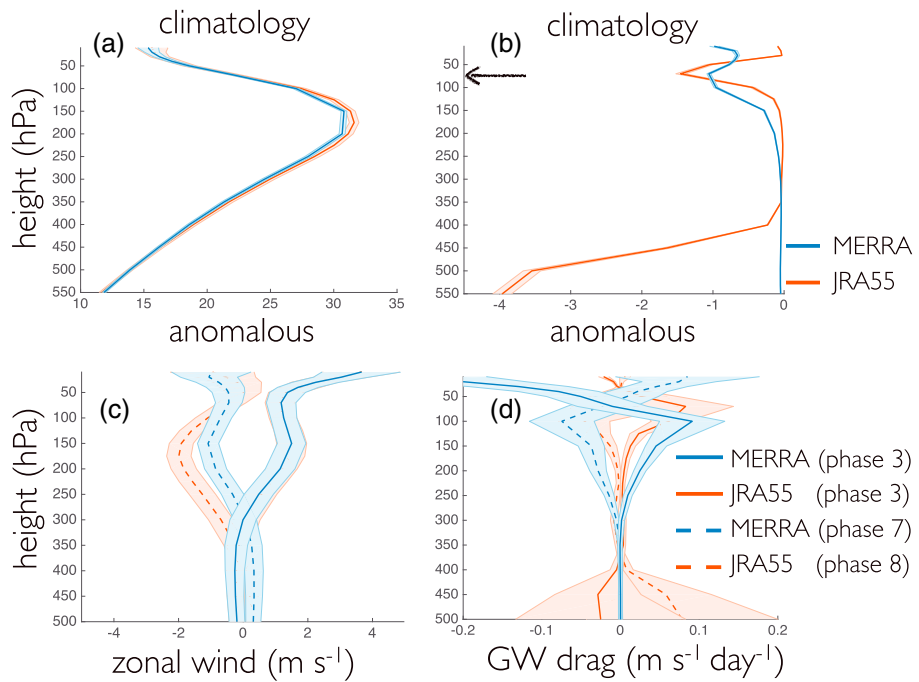


Figure 3. Vertical structures of wind and GW drag anomalies, illustrating the mechanism of interaction. The vertical profiles of zonal wind and GW drag shown here were averaged above the Tibetan Plateau (top brown rectangle in Figure 1) using both the MERRA and JRA55 reanalysis data sets. (a and b) The climatological profiles of zonal wind and GW drag, respectively. (c and d) Deviations from the climatology of zonal wind and GW drag, respectively, during early and late MJO phases. Solid and dashed lines mark the mean profiles, while the 95% confidence interval about the mean is shaded. The black arrow in Figure 3b marks the height at which the Froude number computed from climatological mean fields, and source at 500 hPa, exceeds one.

During phase 3, enhanced convection occurs over the Indian Ocean and anomalous eastward acceleration by GW breaking occurs at 100 hPa over the Tibetan Plateau (Figure 2c). Remember that enhanced GW breaking produces a stronger westward acceleration, so reduced GW breaking over Tibet is occurring when equatorial convection is enhanced in MJO phase 3. Opposite signed anomalies of convection and GW breaking occur during MJO phase 7 (Figure 2d).

4. Simple Mechanism for the Interaction

We argue that GW breaking is modulated through the MJO's effect on upper level horizontal winds over Tibet. Upper tropospheric anticyclones accompany equatorial precipitation in the MJO on each side of the equator [Cassou, 2008; Rui and Wang, 1990]; these Rossby gyres are consistent with the linear response to equatorial latent heating by precipitation and extend thousands of kilometers off the equator [Gill, 1980]. Enhanced equatorial convection in MJO phase 3 is accompanied by anomalous eastward flow at 100 hPa over Tibet that is part of such a Rossby gyre (Figure 2c; the vorticity associated with these gyres is shown in Figure S3).

Both MERRA and JRA55 estimate GW-mediated momentum transfers [McFarlane, 1987; Iwasaki et al., 1989] using linear theory that predicts wave breaking in critical layers (regions where wave phase speeds match the mean flow speed) and using estimates of when nonlinear processes (e.g., convective instability) initiate [Andrews et al., 1987; Fritts and Alexander, 2003]. During boreal winter the mean zonal wind is far above zero throughout the troposphere and stratosphere over Tibet (Figure 3a), so there are no critical layers for stationary GWs, and it is the latter process of nonlinear wave saturation that is relevant here. In particular, vertically propagating waves amplify with height due to the exponential decrease in air density; convective stability is maintained when horizontal winds increase with height rapidly enough to prevent streamlines in the wave-modified flow from folding over. This stability condition is approximated to hold when $Fr \leq 1$, with the nondimensional local Froude number Fr defined as

$$Fr = \left(\frac{Nh}{U} \right) \sqrt{\frac{\rho_0 N_0 U_0}{\rho N U}},$$

where h is amplitude of the orographic perturbation, ρ is air density, N is stratification, U is mean flow speed, and zero subscripts denote values at the wave source level. Below the peak eastward wind, which occurs around 175 hPa in the climatological mean during boreal winter, GWs amplify with height but do not break because of the increase in eastward winds. But at higher levels, ρ and U both decrease so that Fr exceeds unity and wave breaking and momentum deposition occur (see supporting information for details on the “wave saturation” approximation used in MERRA and JRA55 to represent wave breaking). This results in the maximum GW drag occurring at 75 hPa in MERRA (Figure 3b); in JRA55 there is a local maximum at 75 hPa, but a much larger maximum exists at low levels due to the fact that GWs with wavelengths around 10 km are assumed to be trapped and dissipate in the troposphere in the JRA55 parameterization [Iwasaki *et al.*, 1989].

The upper level Rossby gyre in the MJO modifies the level at which zonal wind speeds decrease sufficiently to allow gravity wave breaking. When precipitation is enhanced over the equatorial Indian Ocean during MJO phase 3, upper level eastward winds are stronger (Figure 3c) and the level at which the Froude number exceeds unity shifts upward. This is associated with a reduction in GW drag (i.e., less westward acceleration) between about 75 hPa and 250 hPa (Figure 3d). There is a region of enhanced GW drag at higher altitudes in MERRA, indicating that the level of wave breaking simply moved upward together with the level at which $Fr = 1$. In JRA55 there is a compensating increase in GW drag at low levels, although the uncertainty of that low-level signal is so large that it is not statistically significant; nevertheless, this low-level increase in GW drag is consistent with the eastward wind weakening at low levels during MJO phase 3 as part of an opposite sign Rossby wave gyre at low levels [Rui and Wang, 1990]. In both data sets, the wind and GW drag anomalies have opposite signs during the MJO phase associated with suppressed equatorial rainfall in the Indian Ocean.

Note that surface wind anomalies are expected to affect the magnitude of the GW source, but the MJO-related changes in surface winds are very small. Furthermore, the change in GW drag above Tibet, vertically integrated above 550 hPa in both MERRA and JRA55 and during all MJO phases, shows no statistically significant change (at a 5% confidence level, see supporting information)—thus, the total drag is approximately conserved. This means that the total, vertically integrated drag over Tibet does not depend on the MJO and that the drag simply shifts up and down with MJO phase.

5. Summary and Conclusions

In summary, a new influence of tropical tropospheric intraseasonal variability on wave propagation into the extratropical stratosphere is identified. Although the MJO and orographic GWs operate in domains traditionally thought to be geographically distinct, their activities are strongly correlated in two different data sets. Estimates of GW drag in the MERRA and JRA55 reanalyses are based on parameterizations rather than direct observations of GW activity, but the mechanism by which the MJO’s upper level gyres seems to influence the vertical propagation of GWs is consistent with simple theory of GW saturation. Our results raise multiple questions about the vertical propagation of GWs into the upper atmosphere. For example, if the number of MJO events increases as Earth’s climate warms [Subramanian *et al.*, 2014; Arnold *et al.*, 2015], how might this affect orographic GW propagation into the upper atmosphere? How accurate are the parameterizations of GW drag that are used in the MERRA and JRA55 reanalyses and might the actual GW drag be much more or less sensitive to the MJO? Our results motivate the collection of more observations of GWs over the Tibetan plateau, more detailed assessment of orographic GW variability on a range of time scales, and development of better understanding of the conditions fostering wave generation and breaking. Lastly, this work emphasizes the importance of local processes over Tibet for circulations that set distributions of high-altitude trace gases (e.g., ozone) which are known to be modulated by the MJO [e.g., Tian and Waliser, 2012].

Acknowledgments

Both authors acknowledge support by Office of Naval Research awards N00014-11-1-0617 and N00014-15-1-2531. Both authors thank Tiffany Shaw, Adam Sobel, Ronald Smith, and Joan Alexander for useful comments and discussion. MERRA data were acquired from the Goddard Earth Science Data Information Services Center, <http://disc.sci.gsfc.nasa.gov/daac-bin/DataHoldings.pl>. JRA55 data files were obtained from the Japan Meteorological Agency, http://jra.kishou.go.jp/JRA-55/index_en.html. NOAA OLR was acquired from NOAA’s National Centers for Environmental Information, <http://www.ncdc.noaa.gov>. MJO phase classifications were obtained from the Australian Bureau of Meteorology, <http://www.bom.gov.au/climate/mjo>.

References

- Andrews, D. G., J. R. Holton, and C. B. Leovy (1987), *Middle Atmosphere Dynamics*, vol. 40, Academic Press, San Diego, Calif.
Arnold, N. P., M. Branson, Z. Kuang, D. A. Randall, and E. Tziperman (2015), MJO intensification with warming in the superparameterized CESM, *J. Clim.*, 28(7), 2706–2724.
Böhler, O. (2014), *Waves and Mean Flows*, Cambridge Univ. Press, Cambridge, U. K.
Butchart, N. (2014), The Brewer-Dobson circulation, *Rev. Geophys.*, 52, 157–184, doi:10.1002/2013RG000448.
Cassou, C. (2008), Intraseasonal interaction between the Madden-Julian oscillation and the North Atlantic oscillation, *Nature*, 455(7212), 523–527.
Cohen, N. Y., E. P. Gerber, and O. Bühl (2014), What drives the Brewer-Dobson circulation?, *J. Atmos. Sci.*, 71(10), 3837–3855.
Fritts, D. C., and M. J. Alexander (2003), Gravity wave dynamics and effects in the middle atmosphere, *Rev. Geophys.*, 41(1), 1003, doi:10.1029/2001RG000106.

- Garfinkel, C. I., S. B. Feldstein, D. W. Waugh, C. Yoo, and S. Lee (2012), Observed connection between stratospheric sudden warmings and the Madden-Julian Oscillation, *Geophys. Res. Lett.*, 39, L18807, doi:10.1029/2012GL053144.
- Garfinkel, C. I., J. J. Benedict, and E. D. Maloney (2014), Impact of the MJO on the boreal winter extratropical circulation, *Geophys. Res. Lett.*, 41, 6055–6062, doi:10.1002/2014GL061094.
- Gill, A. (1980), Some simple solutions for heat-induced tropical circulation, *Q. J. R. Meteorol. Soc.*, 106, 447–462.
- Iwasaki, T., S. Yamada, and K. Tada (1989), A parameterization scheme of orographic gravity wave drag with two different vertical partitionings. I: Impacts on medium-range forecasts, *J. Meteorol. Soc. Jpn.*, 67(1), 11–27.
- Kobayashi, S., et al. (2015), The JRA-55 reanalysis: General specifications and basic characteristics, *J. Meteorol. Soc. Jpn.*, 93(1), 5–48.
- Lau, W. K.-M., and D. E. Waliser (2011), *Intraseasonal Variability in the Atmosphere-Ocean Climate System*, Springer, Berlin.
- Liebmann, B. (1996), Description of a complete (interpolated) outgoing longwave radiation dataset, *Bull. Am. Meteorol. Soc.*, 77, 1275–1277.
- Liu, C., Y. Liu, Z. Cai, S. Gao, D. Lü, and E. Kyrölä (2009), A Madden-Julian Oscillation-triggered record ozone minimum over the Tibetan Plateau in December 2003 and its association with stratospheric “low-ozone pockets”, *Geophys. Res. Lett.*, 36, L15830, doi:10.1029/2009GL039025.
- Madden, R. A., and P. R. Julian (1971), Detection of a 40–50 day oscillation in the zonal wind in the tropical Pacific, *J. Atmos. Sci.*, 28(5), 702–708.
- Madden, R. A., and P. R. Julian (1994), Observations of the 40–50-day tropical oscillation—A review, *Mon. Weather Rev.*, 122(5), 814–837.
- McFarlane, N. (1987), The effect of orographically excited gravity wave drag on the general circulation of the lower stratosphere and troposphere, *J. Atmos. Sci.*, 44(14), 1775–1800.
- Onogi, K., et al. (2007), The JRA-25 reanalysis, *J. Meteorol. Soc. Jpn.*, 85(3), 369–432.
- Rienecker, M. M., et al. (2011), MERRA: NASA's Modern-Era Retrospective Analysis for Research and Applications, *J. Clim.*, 24(14), 3624–3648.
- Rui, H., and B. Wang (1990), Development characteristics and dynamic structure of tropical intraseasonal convection anomalies, *J. Atmos. Sci.*, 47(3), 357–379.
- Subramanian, A., M. Jochum, A. J. Miller, R. Neale, H. Seo, D. Waliser, and R. Murtugudde (2014), The MJO and global warming: A study in CCSM4, *Clim. Dyn.*, 42(7–8), 2019–2031.
- Tian, B. J., and D. E. Waliser (2012), *Chemical and Biological Impacts. Chapter 18 in Intraseasonal Variability of the Atmosphere-Ocean System (2nd Edition)*, edited by K.-M. Lau and D. E. Waliser, pp. 569–585, Springer, Heidelberg, Germany.
- Virts, K. S., and J. M. Wallace (2014), Observations of temperature, wind, cirrus, and trace gases in the tropical tropopause transition layer during the MJO, *J. Atmos. Sci.*, 71(3), 1143–1157.
- Weare, B. C. (2010), Madden-Julian Oscillation in the tropical stratosphere, *J. Geophys. Res.*, 115, D17113, doi:10.1029/2009JD013748.
- Wheeler, M. C., and H. H. Hendon (2004), An all-season real-time multivariate MJO index: Development of an index for monitoring and prediction, *Mon. Weather Rev.*, 132(8), 1917–1932.
- Zhang, C. (2005), Madden-Julian Oscillation, *Rev. Geophys.*, 43, RG2003, doi:10.1029/2004RG000158.

Supporting Information for “Modulation of subtropical stratospheric gravity waves by equatorial rainfall”

Naftali Y. Cohen and William R. Boos

Department of Geology and Geophysics, Yale University, New Haven,
Connecticut

Contents of this file

1. Text S1 to S5
2. Figures S1 to S4
3. Table S1

Introduction This is supplementary material to the main text, containing additional discussion and several alternative analyses. In addition, here we provide more detailed quantification of some analyses presented in the main text.

Text S1. Figure S1 shows a time series of daily GW drag anomalies over Tibet and OLR anomalies over the near-equatorial Indian ocean during the winter of 1987-88. The

Corresponding author: Naftali Y. Cohen, Department of Geology and Geophysics, Yale University, P. O. Box 208109, New Haven, CT 06520-8109. E-mail: naftalic@gmail.com

amplitude of the daily GW drag anomalies reaches $\pm 6 \text{ m s}^{-1} \text{ day}^{-1}$. These GW drag variations are large and, as seen in the figure, negatively correlated with equatorial OLR during MJO phases 3 and 7. Thus, although the *ensemble mean* fluctuations of GW drag are relatively small (e.g. Fig. 2 and Fig. S2), anomalies in *individual* MJO events can be quite large.

Text S2. Figure S2 complements Figs. 2a, b of the main text by showing the same scatter plot, but using only “highly-defined” MJO events (panels a, b) and then using OLR data from the MERRA and JRA55 datasets instead of NOAA satellites (panels c, d).

Text S3. Figures S3a, b complement Figs. 2c, d of the main text by showing the vorticity gyres (in blue contours) that accompany the active and suppressed phases of the MJO.

Table S1. Table S1 summarizes the statistical analysis of Figs. 2a, b and Fig. S2. It shows that the linear regression lines (the black lines) have statistically significant negative slopes and that the correlations between GW drag averaged over the Tibetan Plateau and top-of-the-atmosphere OLR averaged over the Indian Ocean are high.

Text S4. We now discuss, in more detail, the argument that the vertically integrated gravity wave drag over Tibet does not change significantly when binned by MJO phase — instead the drag gets distributed differently with height (i.e. it shifts up or down). The idea is simply that if the force applied by the atmosphere on topography *at the source level* over Tibet does not depend on the MJO, then the column-integrated force (binned by MJO phase) also should not change. We find that the vertically integrated drag anomalies that are associated with the different MJO phases are not distinguishable from zero (at

a 5% confidence level). For example, the MERRA drag anomaly spatially integrated (above 400 hPa and over the northern box in Fig. 1) during phase 3 has a 95% confidence interval of -1.83 to $+1.13 \times 10^{11}$ N, while during phase 7 its 95% confidence interval is -1.89 to $+1.08 \times 10^{11}$ N. Thus, the integrated drag anomalies are indistinguishable from zero. Similarly, the JRA55 integrated drag anomalies during phases 3 and 8 have confidence intervals of -2.77 to $+2.77 \times 10^{11}$ N and -3.31 to $+3.10 \times 10^{11}$ N, respectively. Note that the number of days with different MJO phases differs, which influences the confidence intervals. For example, there are 388 days of phase 3, 479 days of phase 7, and only 334 days of phase 8 during the boreal winters of 1979-2012.

Text S5. We now discuss in more detail the conditions for GW breaking in both MERRA and JRA55 parameterizations of GW drag, which are based on methods presented by *McFarlane* [1987]. Far from the dissipation region, the GW amplitude is $A = h(\rho_0 N_0 U_0 / \rho N U)^{1/2}$, with symbols defined in the main text. Thus, as GWs propagate upward their amplitudes grow exponentially because of the density decrease. Below the jet maximum, amplitude growth is limited by an increase in the wind speed with height (Fig. 3a), but above the jet maximum the wave amplitude grows exponentially as density and wind speed both decrease. The onset of convective instability leads to turbulent dissipation of wave energy, and a saturation approximation assumes that this turbulence leads to momentum transport that limits the wave amplitude. Multiplying the wave amplitude by an exponentially decaying function parameterizes this process.

More precisely, the onset of convective instability in linear theory occurs when the vertical gradient of the potential temperature becomes negative. This results in a simple

condition that the local Froude number $Fr = NA/U$ exceeds one (note that the Froude number is often written as NH/U , where H is a length scale associated with the mean flow, but here the local Froude number uses h , which is the amplitude of the orographic perturbation). The local Froude number is a function of height and its typical vertical structure during winter above Tibet is illustrated in Fig. S4a using MERRA data. Here, U , ρ and N are taken from the reanalysis data, h is estimated to be 1 km and the source level is taken to be at 500 hPa (which is near the surface over the Tibetan Plateau). One can see that the extratropical jet is centered at about 150 hPa and that the stratification N has a relatively mild vertical variation about the value of 0.01 s^{-1} . The density of the flow decreases exponentially with height. Below about 150 hPa the Froude number is small as the increase in zonal wind compensates for the decrease in the density. However, above the jet maximum both the density and the zonal wind contribute to amplify the Froude number. This results in GW dissipation and momentum deposition (i.e. “wave breaking” or “drag”) that limit the wave amplitude and prevent the occurrence of actual convective instability. Indeed, the stratification (a measure of convective stability) remains largely fixed as the Froude number increases.

In order to further illustrate how the mean flow conditions and GW breaking (over Tibet) are modified due to MJO activity, we estimate the Froude number during phases 3 and 7 using the mean U profiles shown in Fig. 3c of the main text. The anomalous Froude number is shown in Fig. S4b: during MJO phase 3, Fr decreases and therefore waves can propagate to higher levels before breaking, whereas during phase 7, Fr increases and more breaking takes place at lower levels in the stratosphere and upper troposphere.

References

- McFarlane, N. (1987), The effect of orographically excited gravity wave drag on the general circulation of the lower stratosphere and troposphere, *Journal of the Atmospheric Sciences*, **44**, 1775–1800.

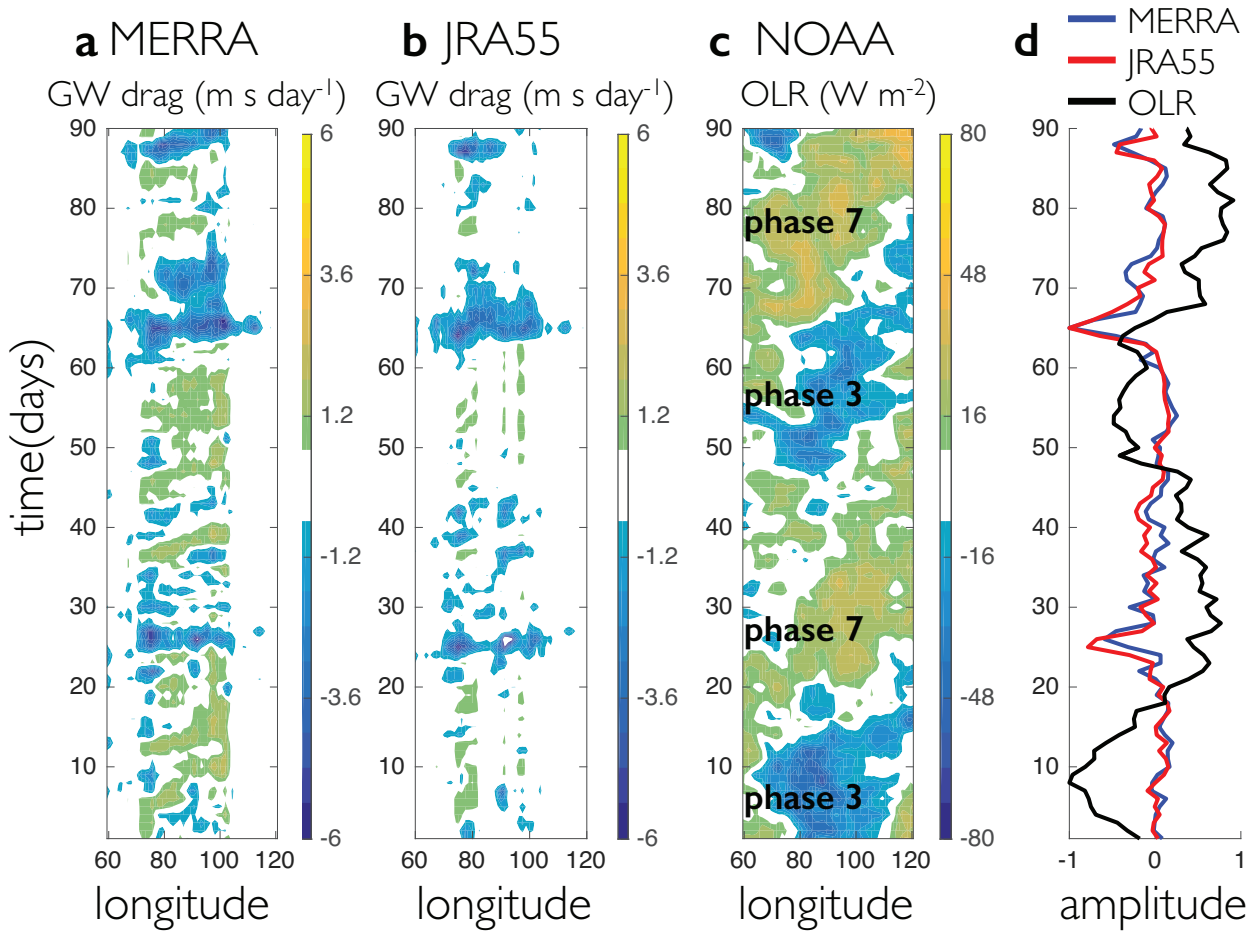


Figure S1. Time series of GW drag anomalies over Tibet and equatorial OLR over the Indian ocean. Panels a and b show anomalies of latitudinal mean GW drag over Tibet (the northern brown rectangle in Fig. 1 of the main text) as a function of time during the winter of 1987-88 using MERRA and JRA55 reanalyses data, while panel c shows anomalies of latitudinal mean NOAA OLR over the Indian ocean (the southern brown rectangle in Fig. 1 of the main text) as a function of time during the winter of 1987-88. Panel d shows the longitudinal average over panels a-c, scaled by the maximum amplitude in each panel.

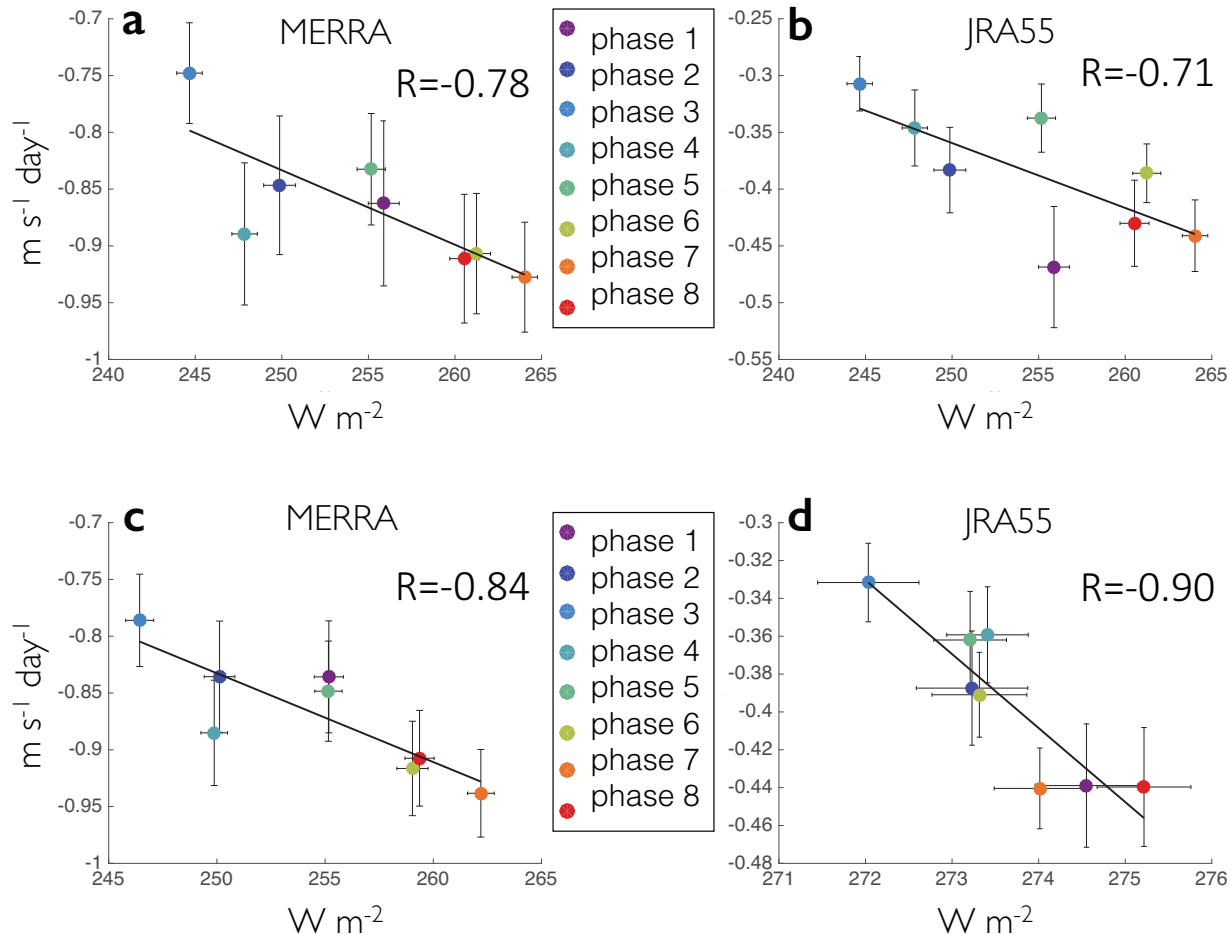


Figure S2. Panels a and b are the same as Figs. 2a, b of the main text, but here MJO events that are not “highly-defined” (see Methods) are omitted from the analysis. In this way there is more certainty about MJO location. Panels c and d are the same as Figs. 2a, b of the main text, but here OLR data is taken from MERRA (panel c) and JRA55 (panel d) instead of NOAA satellites.

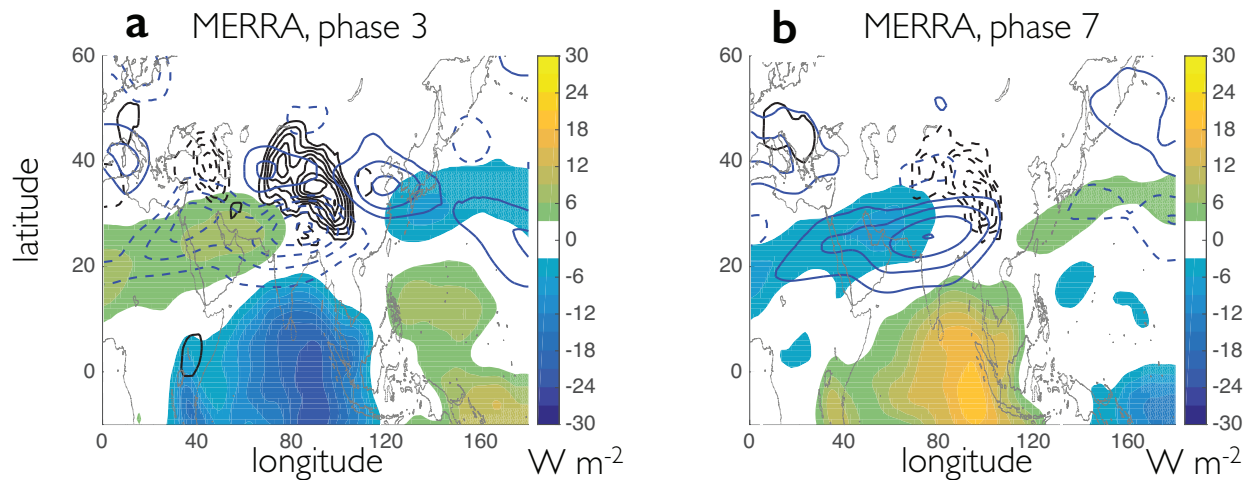


Figure S3. Panels a and b are the same as Figs. 2c, d of the main text but with the blue contours showing the anomalies in Ertel's potential vorticity at 200 hPa (contour interval of 10^{-7} K m² kg⁻¹ s⁻¹, negative dashed) instead of zonal wind.

Table S1. The linear regression slopes between the GW drag and OLR in MERRA and JRA datasets.

	Linear regression slope between the GW drag and OLR (with 95% confidence bounds)	Pearson's R	SSE
MERRA (Fig. 2a)	-0.0060 (-0.0103, -0.0017)	-0.81	0.0063
JRA55 (Fig. 2b)	-0.0050 (-0.0085, -0.0015)	-0.82	0.0041
MERRA (Fig. S2a)	-0.0066 (-0.0117, -0.0014)	-0.78	0.0091
JRA55 (Fig. S2b)	-0.0057 (-0.0114, -0.0001)	-0.71	0.0110
MERRA (Fig. S2c)	-0.0078 (-0.0130, -0.0027)	-0.84	0.0055
JRA55 (Fig. S2d)	-0.0391 (-0.0583, -0.0199)	-0.90	0.0024

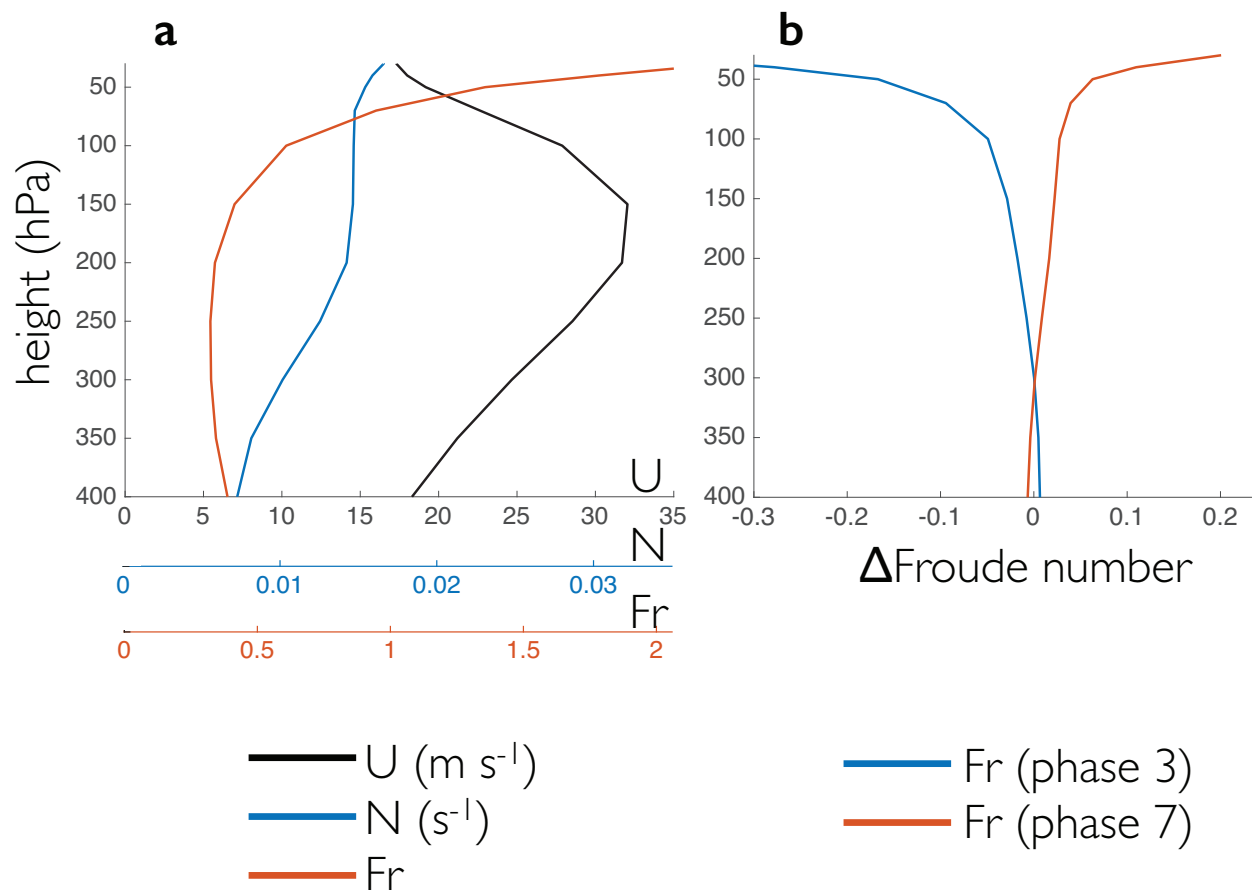


Figure S4. Panel a shows the vertical structure of the local Froude number computed using time-mean winter conditions over the Tibetan Plateau, while panel b shows the change in the vertical structure of the local Froude number for MJO phases 3 and 7 during the winter, all using MERRA data for 1979-2012.